Bond-order potential for the surface-terminated titanium carbide MXene monolayers $\mathrm{Ti}_{n+1}\mathrm{C}_n T_x$ (n=1, 2, or 3; T = -O or -F)

Gabriel Plummer [1], Siby Thomas [1,2] Mohsen Asle Zaeem [1], and Garritt J. Tucker [1,*]

[1]*Department of Mechanical Engineering, Colorado School of Mines, Golden, Colorado 80401, USA*
[2]*Department of Electrical and Computer Engineering, Technical University of Munich, Karlstrasse 45-47, 80333 Munich, Germany*

MXenes are an emerging family of two-dimensional (2D) materials with highly tunable properties. Their fundamental mechanical properties have received comparatively less research attention than other functional properties due to the difficulty of performing such experiments on 2D materials. Therefore, we have developed a bond-order potential for surface-terminated titanium carbide MXene monolayers ($\mathrm{Ti}_{n+1}\mathrm{C}_n T_x$, $n = 1$, 2, or 3, T = -O or -F), enabling large-scale atomistic simulations which can probe both mechanical properties and deformation mechanisms. The bond-order potential does an excellent job of capturing relevant structural, elastic, and defect properties of the studied MXenes with and without surface terminations and is computationally scalable to allow for molecular dynamics simulations of monolayers hundreds of nanometers in size, only an order of magnitude below typical monolayer experiments. Crucially, these large-scale simulations open the possibility to study more realistic MXenes containing distributions of both defects and nonuniform surface terminations. We demonstrate in this work that these variables can have significant effects on the mechanical response of MXenes and therefore offer additional property-tuning capabilities which can be utilized to inform synthesis and postprocessing techniques.

I. INTRODUCTION

MXenes are a large family of two-dimensional (2D) early transition metal carbides and/or nitrides which have attracted considerable attention over the past decade for their unique and tunable properties [1]. This tunability has set them apart from other 2D materials and has led to significant research activity focused on their use in applications such as energy storage [2], catalysis [3,4], electronic devices [5], sensors [6,7], structural composites [8], and more. MXenes, which are synthesized via the selective etching of the A element in MAX phase precursors [9], take on the chemical formula $M_{n+1}X_nT_x$, where M is an early transition metal, X is either carbon or nitrogen, T is a surface termination group (commonly, -O, -F, or -OH), and n denotes the monolayer thickness (Fig. 1). Their tunability arises from the ability to substitute and/or combine numerous different species at the M, X, and T sites while retaining the 2D MXene structure.

Mechanical properties play a crucial role in nearly all applications currently being studied for MXenes. Despite this, the fundamental mechanical behavior of MXenes has received significantly less research attention than other areas [10]. This can partly be attributed to the difficult and time-consuming nature of mechanical characterization experiments on 2D materials; only a few studies have been conducted thus far on

MXene monolayers [11,12]. In place of additional experiments, numerous density functional theory (DFT) calculations have been able to provide valuable details about the mechanical properties of various MXene compositions [13–18]. DFT calculations, however, are limited to a few hundred atoms at most, which precludes the study of more realistic MXenes, which are known to contain heterogeneities such as vacancies [19] and nonuniform surface terminations [20,21], as well as the study of deformation mechanisms occurring at length scales greater than a few unit cells.

This length-scale limitation of DFT can be overcome with atomistic simulations, which make use of empirical interatomic potentials and are able to model orders of magnitude larger systems. As such, several interatomic potentials have previously been developed for titanium carbide MXenes, the most studied system to date. It is important to note, however, that the empirical nature of these models means they must be rigorously validated to ensure an accurate description of the system(s) and phenomena of interest. Borysiuk *et al.* utilized a hybrid-style potential to model the mechanical behavior of titanium carbide MXenes without surface terminations (pristine) [22,23] and successfully studied the deformation of monolayers up to about 40 nm in size. With this being the first potential developed for MXenes, however, it lacks thorough validation with respect to relevant MXene properties. Osti *et al.* developed a parametrization of ReaxFF to study intercalation dynamics in surface-terminated titanium carbide MXenes [24]. The use of this ReaxFF potential has since been extended to studying the mechanical behavior of both monolayer and multilayer MXenes [25–27]. Despite not being originally developed for these types of simulations, the ReaxFF parametrization has been the best option for
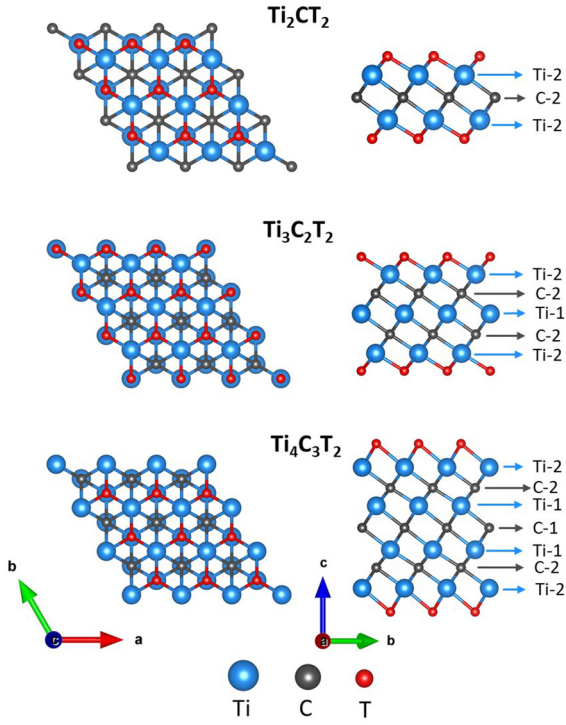
*tucker@mines.edu

FIG. 1. Top and side views of the crystalline structure of surface-terminated titanium carbide MXene monolayers. Ti and C layers are labeled according to their proximity to the surface. T represents surface terminations of -O or -F.

performing atomistic simulations of MXene deformation. The functional form of ReaxFF is quite computationally expensive, however, and is suitable for studying complex chemical interactions at small scales but undesirable for large-scale studies of deformation [28].

Given the aforementioned challenges, herein we have developed a bond-order potential (BOP) for surface-terminated MXene monolayers which provides an accurate description of relevant MXene properties while retaining enough simplicity to enable simulations an order of magnitude larger than has previously been possible with ReaxFF. We have chosen the titanium carbide MXene system (Fig. 1) as it is currently the most studied MXene, and significant experimental and computational data are available—notably only one BOP parametrization is able to successfully model three different $Ti_{n+1}C_nT_x$ monolayers ($n = 1$, 2, and 3). The inclusion of interactions for both -O and -F surface terminations now enables large-scale simulations of more realistic MXene monolayers with experimentally guided distributions of both vacancies and nonuniform surface terminations. Thus, the effects of these heterogeneities on MXene mechanical properties and deformation mechanisms can now be studied at a level of detail not previously possible.

II. BOND-ORDER INTERATOMIC POTENTIAL AND FITTING PROCEDURE

In previous work [29,30] we utilized Tersoff-style BOPs [31] to successfully model multiple titanium carbide–containing MAX phases, the ternary precursors to MXenes.
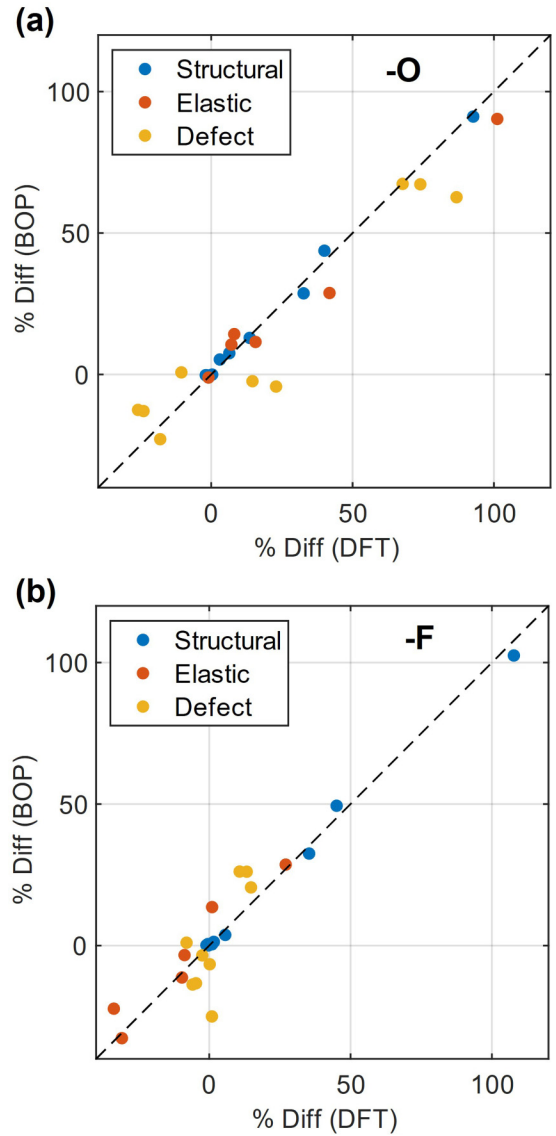

FIG. 2. Results from fitting surface termination interactions for both -O and -F groups. Percent differences of material properties with respect to the pristine MXenes are plotted for BOP calculations against DFT calculations. Structural properties include in-plane lattice constants, monolayer thicknesses, and cohesive energies. Elastic properties include the in-plane elastic constants. Defect properties include Ti and C vacancy formation energies.

Therefore, developing similar potentials for their binary MXene derivatives is a natural extension. The formalism and physical basis of the specific BOP used herein is described in detail in Ref. [32]. Briefly, summing over all i-j atom pairs, the energy functional takes the following form:

$$E = \frac{1}{2} \sum_i \sum_{j \neq i} f_{ij}^C(r_{ij})\left[f_{ij}^R(r_{ij}) + b_{ij} f_{ij}^A(r_{ij})\right], \qquad (1)$$

where f_{ij}^C is a cutoff function, f_{ij}^R and f_{ij}^A are repulsive and attractive two-body terms, respectively, and b_{ij} is a many-body term called the bond-order parameter, which accounts for the angular dependence of bonds and couples the coordination environment to bond strength. The smooth cutoff function
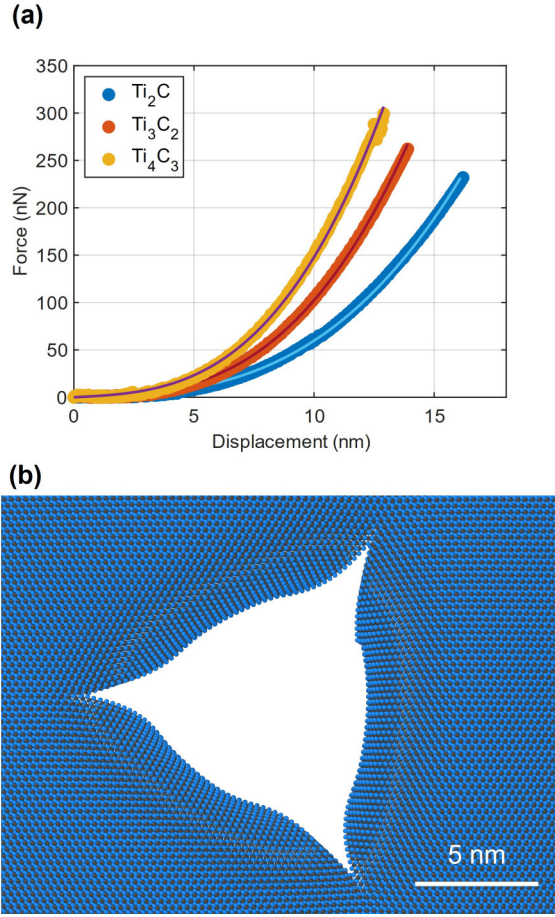
(a)

(b)

FIG. 3. (a) Examples of force-displacement curves generated from nanoindentation simulations of 100 nm diameter pristine MXene monolayers. Atomistic data (points) are overlaid with fits to Eq. (9) (lines). (b) A typical threefold symmetric fracture pattern observed during nanoindentation simulations in a 50 nm diameter Ti_3C_2 monolayer. Atoms are colored by type: Ti, blue; C, gray.
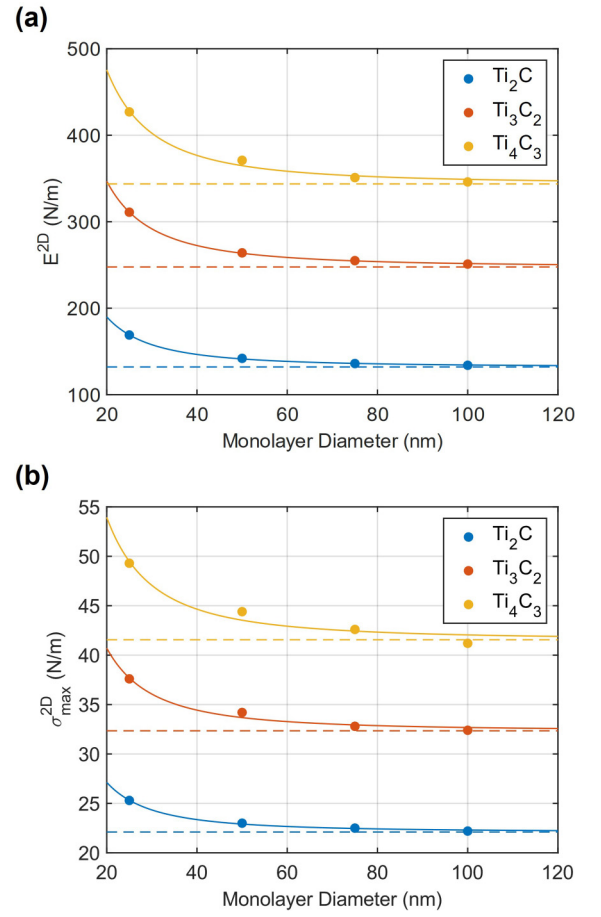
(a)

(b)

FIG. 4. Values for the 2D elastic modulus and breaking strength extracted from fitting atomistic nanoindentation data to Eq. (9) plotted as a function of monolayer diameter. Solid lines represent asymptotic fits to Eq. (12). Dashed lines represent the asymptote approached by the data.

is defined by the following equation with free parameters R and D:

$$f_{ij}^C(r_{ij}) = \begin{cases} 1 & r_{ij} < R - D, \\ \frac{1}{2} - \frac{1}{2}\sin\left(\frac{\pi}{2}\frac{r_{ij}-R}{D}\right) & R - D < r_{ij} < R + D, \\ 0 & r_{ij} > R + D. \end{cases} \quad (2)$$

Typically, R and D are defined such that only first nearest neighbors fall within the cutoff range. This is the case here, with the exception of Ti-Ti interactions, which become second-nearest neighbors in the titanium carbide MXene structure. The two-body terms are taken as Morse-style potentials with free parameters A, λ_1, B, and λ_2:

$$f_{ij}^R(r_{ij}) = A\exp\left(-\lambda_1 r_{ij}\right), \quad (3)$$

$$f_{ij}^A(r_{ij}) = -B\exp\left(-\lambda_2 r_{ij}\right). \quad (4)$$

The bond-order term, which sums over all k atoms influencing the i-j pair in a bond-order sense, is given by

$$b_{ij} = (1 + \zeta_{ij})^{-\frac{1}{2}}, \quad (5)$$

$$\zeta_{ij} = \sum_{k\neq i,j} f_{ik}^C(r_{ik})g_{ik}(\theta_{ijk})\exp\left[\lambda_{3,ijk}(r_{ij} - r_{ik})\right], \quad (6)$$

$$g_{ik}(\theta_{ijk}) = \gamma\left(1 + \frac{c^2}{d^2} - \frac{c^2}{d^2 + (\cos\theta_{ijk} - h)^2}\right), \quad (7)$$

where γ, c, d, and h are free parameters associated with bond angles, λ_3 is associated with relative bond lengths, and θ_{ijk} is the angle between bonds i-j and i-k. In principle, these parameters can be defined for each three-body permutation in the system of interest, but in practice they are typically defined only for pairs (note the notation g_{ik} rather than g_{ijk} for the angular function). The exception here is the λ_3 parameter, for which we define values according to all three atoms in the triplet. This approach has proven effective in other carbide systems employing the same potential form due to the combination of first- and second-nearest-neighbor interactions [33].

In total, a pristine MXene potential with Ti-Ti, C-C, and Ti-C interactions employing this form requires 36 free parameters to be fitted (see Tables VII and VIII for a full list). The Ti-Ti and C-C parameters are adopted from Refs. [29,34], respectively, leaving 14 parameters associated with Ti-C in-
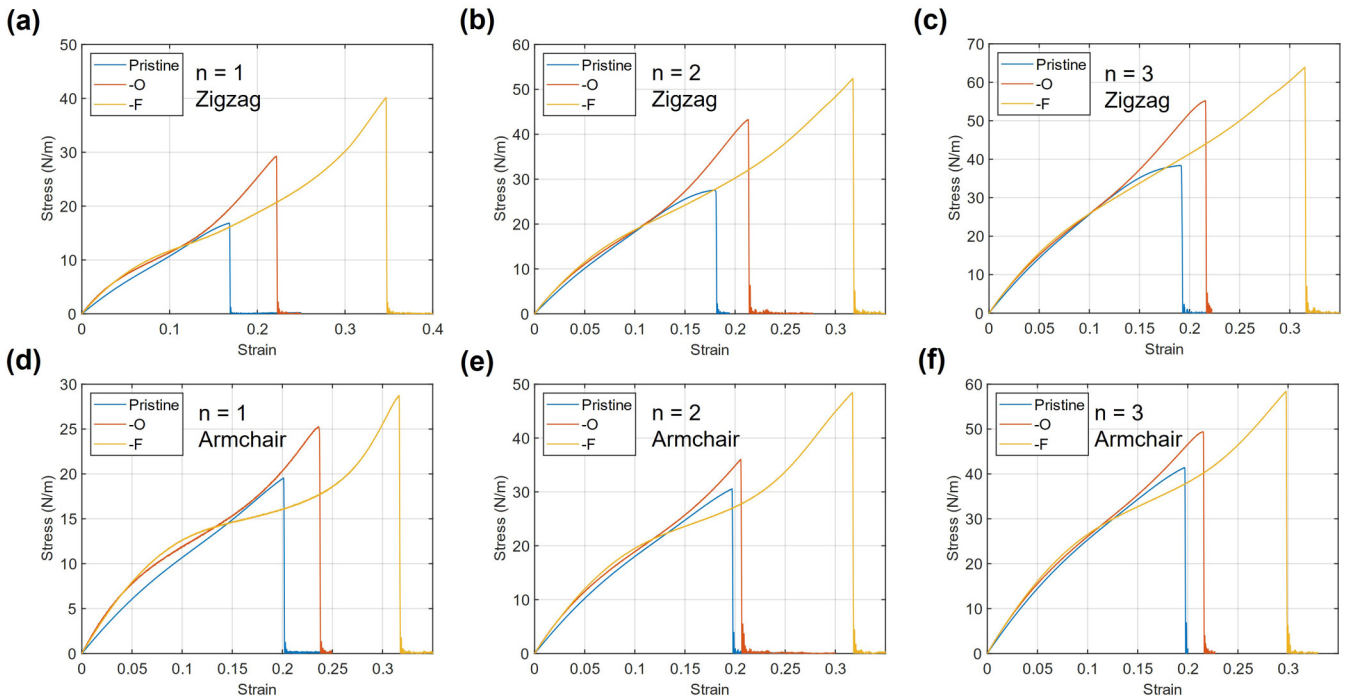
FIG. 5. Stress-strain curves generated from uniaxial tension simulations of both pristine and surface-terminated MXene monolayers. Simulations were performed in two different loading directions: (a)–(c) zigzag and (d)–(f) armchair.

teractions to be fitted to MXene properties. The addition of surface terminations is accomplished by considering Ti-T interactions, which requires an additional 14 binary interaction parameters and 2 new ternary interaction parameters for each surface termination group (see Tables VIII and IX for a full list). The C-T interactions are neglected as they fall outside typical cutoff ranges (a similar strategy was successfully applied to C-*A* interactions in MAX phases [29]). T-T interaction parameters, adopted from Ref. [35], are included in the potential for completeness, but these interactions also fall outside typical cutoff ranges and therefore do not play a role in the MXene structures considered here.

MXene fitting properties were calculated via DFT using the VASP package [36]. The different atomic interactions were governed by the Perdew-Burke-Ernzerhof functional using the generalized gradient approximation approach [37]. Electron-ion interactions were modeled by the projector augmented-wave potentials [38]. The Brillouin zone sampling was created using the Monkhorst-Pack scheme with a grid size of $7 \times 7 \times 1$ (for a $3 \times 3 \times 1$ MXene supercell). The plane wave cutoff for the whole calculation was set as 500 eV. The full optimization of atoms was performed by keeping convergence criteria of 10^{-6} eV and 10^{-3} eV/Å for the total energy and residual force, respectively. During calculations,
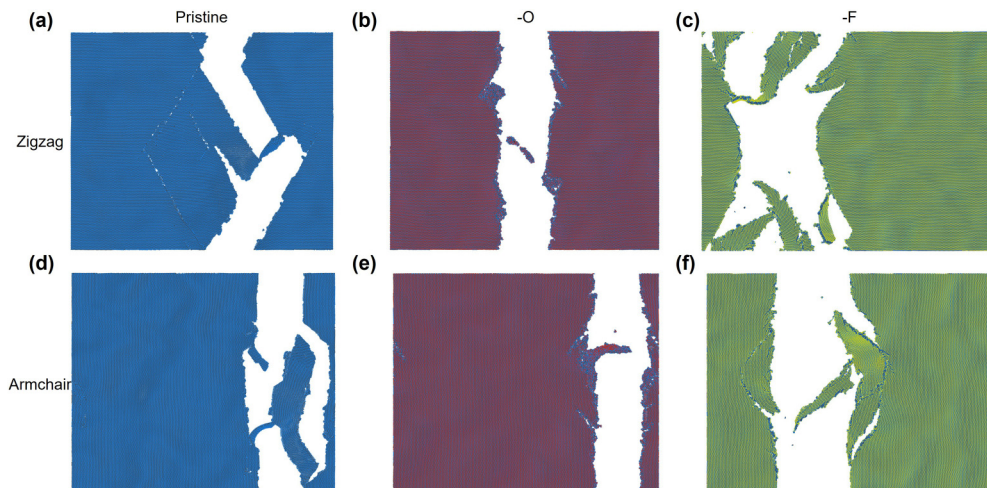

FIG. 6. Snapshots from uniaxial tension simulations on Ti_3C_2 and $Ti_3C_2T_2$ MXene monolayers showing fracture. Atoms are colored by type: Ti, blue; C, gray; O, red; F, yellow.
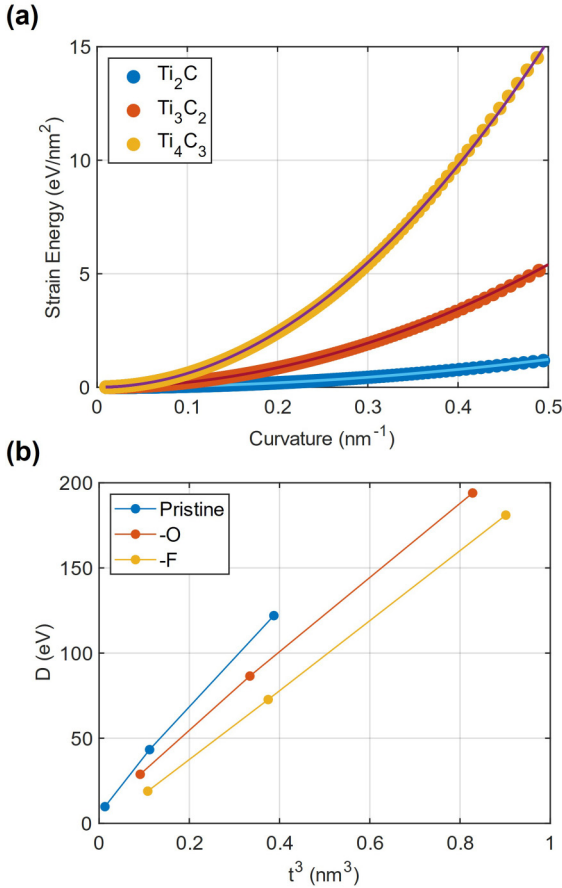
(a)

(b)

FIG. 7. (a) Examples of strain energy plotted as a function of curvature from bending simulations of pristine MXene monolayers. Atomistic data (points) are overlaid with fits to Eq. (13) (lines). (b) Calculated bending rigidity plotted as a function of thickness cubed for both pristine and surface-terminated monolayers.

broadening was controlled by Gaussian smearing using a width of 0.05 eV. A vacuum space of 30 Å was employed along the c axis to avoid interlayer interactions during the periodic DFT calculations.

We utilize the same iterative fitting procedure outlined in our previous work on MAX phase BOPs [29], in which individual interactions, i.e., Ti-C and Ti-T in this case, were fitted by minimizing the sum of squared residuals for a selection of relevant properties, utilizing a simplex search method [39]. The residuals were normalized by tolerance values, which essentially function as weighting parameters during the optimization. Typical tolerance values used were 0.03 Å, 5 GPa, and 0.1 eV. The properties fitted to, for both pristine and surface-terminated MXenes, are the in-plane lattice parameter, monolayer thickness, cohesive energy, in-plane elastic constants, and vacancy formation energies of Ti and C (see Fig. 1 for the labeling convention of different Ti and C sites). Vacancy formation energy is defined via [40,41]

$$E_f = E_{\text{def}} - E_{\text{perf}} + \sum_i n_i \mu_i, \qquad (8)$$

where E_{def} and E_{perf} are the total energies of the defective and defect-free structures, respectively, n_i is the change in the number of atoms of element i, and μ_i is the chemical

potential of element i. Here the chemical potential is taken as the energy of isolated Ti and C atoms rather than that of bulk phases (graphite and hcp Ti) as is typically performed. This allows for a more direct comparison between the relevant DFT and BOP energies. Rather than using the absolute values of material properties to fit the surface termination interactions, the percent changes from pristine properties were used, so that the BOP best captures the influence of various termination groups. Property calculations of the BOP during fitting were performed using LAMMPS, an open source molecular dynamics code [42]. The fitting was carried out in two separate phases of optimization: the first phase, a rough optimization, included structural parameters and cohesive energy, and the second phase, a more stringent optimization, added in elastic constants and defect energies. To best approach a global minimum, this process was repeated with 1000 different parameter initializations, randomly generated within predefined ranges informed by previously developed BOP parameter sets. The fitted parameters are shown in the Appendix.

Table I shows the fitting results for pristine titanium carbide MXenes, and the BOP parametrization does a very good job of capturing the structural, elastic, and defect properties of all three systems. All structural properties fall within 3% of the DFT-calculated values, C_{11} elastic constants within 2%, C_{12} elastic constants within 20%, and defect properties within 12%. Figure 2 summarizes the fitting results for surface terminations. For both the -O and -F groups, the BOP is able to capture the important property trends imparted by the inclusion of surface terminations. Changes in the structural and elastic properties are represented quite well in particular. Full results for fitting of the surface termination interactions can be found in Tables S1 and S2 in the Supplemental Material [43]. For additional validation, we have also performed phonon dispersion calculations for all nine pristine and surface-terminated MXenes (Figs. S1 and S2 [43]), utilizing the PHONOPY [44] and FIXPHONON [45] codes for DFT and BOP calculations, respectively. Both the DFT and BOP calculations are broadly consistent with previously published results for titanium carbide MXenes and importantly exhibit no dynamic instabilities (negative, i.e., imaginary, frequencies) [16]. The acoustic branches predicted by the BOP are generally in good agreement with DFT, but there is more disagreement with the optical branches as the BOP generally predicts higher frequencies, especially with the introduction of surface terminations. As such, this may preclude the BOP from detailed studies of thermal transport in MXenes but should not take away from its capabilities regarding deformation, validation of which is the focus of the remainder of this paper.

III. LARGE-SCALE SIMULATIONS

To complement the material properties fitted to, several large-scale atomistic simulations were performed to demonstrate the capability of the BOP in modeling MXene deformation. These include nanoindentation, uniaxial tension, and bending, which together provide important information on both in-plane and out-of-plane elasticity as well as fracture behavior. As was the case for fitting, atomistic simulations were performed using LAMMPS. Visualizations of simulations were created with the open source software OVITO [46].
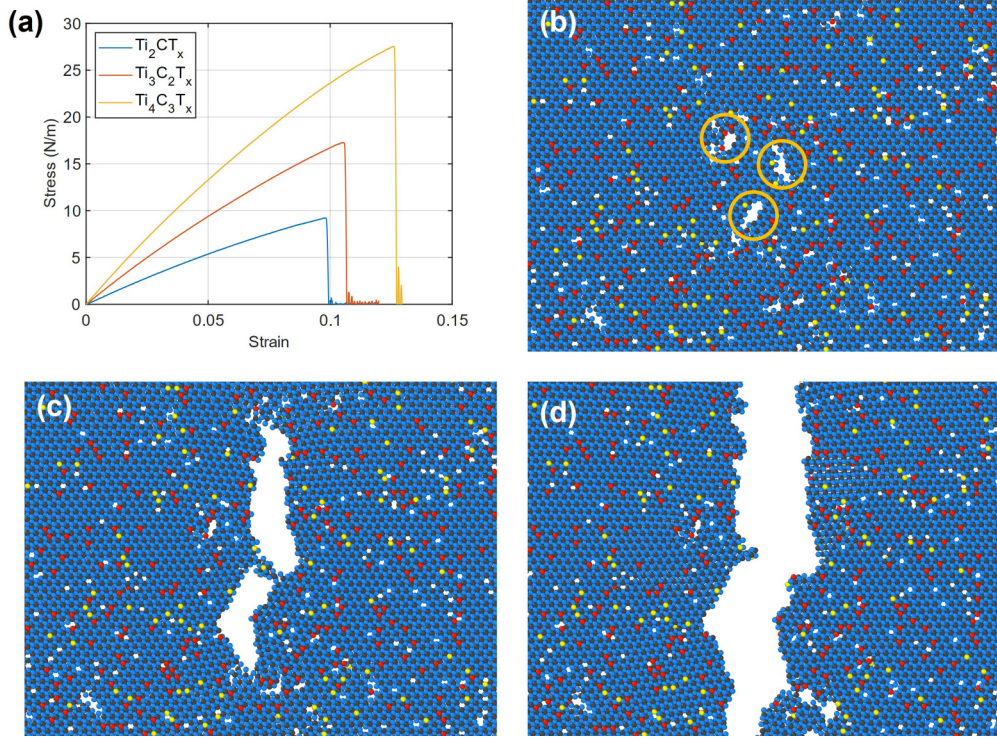
FIG. 8. (a) Representative stress-strain curves from uniaxial tension simulations of defected MXene monolayers. (b)–(d) Snapshots of a Ti_2CT_x monolayer depicting the nucleation and propagation of a crack during uniaxial tension. Orange circles in (b) show vacancy clusters where a crack nucleates. Atoms are colored by type: Ti, blue; C, gray; O, red; F, yellow.

A. Nanoindentation

Nanoindentation simulations are intended to mimic those performed experimentally via atomic force microscopy (AFM) on a number of 2D materials, including MXenes [11,12,47,48]. In this setup a 2D material is positioned over a substrate with circular holes and subsequently indented in its center by an AFM tip. This method produces a force-displacement curve, from which material properties such as the in-plane elastic modulus and breaking strength can be extracted by applying a continuum model [47]:

$$F(\delta) = \sigma_0^{2D} \pi \delta + E^{2D} q^3 a^{-2} \delta^3, \qquad (9)$$

where a is the radius of the circular hole and q is a function of the material's Poisson's ratio: $q = 1/(1.049 - 0.15\nu - 0.16\nu^2)$. The fitting parameters are σ_0^{2D}, which corresponds to pretension in the 2D film, and E^{2D}, a 2D elastic modulus related to the three-dimensional (3D) Young's modulus through film thickness ($E = E^{2D}/t$). Breaking strength, a 2D analog to 3D intrinsic strength, can also be determined from the force-displacement curve:

$$\sigma_{\max}^{2D} = \sqrt{\frac{F_f E^{2D}}{4\pi r_{\mathrm{tip}}}}, \qquad (10)$$

TABLE I. Calculated properties of pristine titanium carbide MXenes using the fitted BOP in comparison with DFT-calculated values. Properties listed are the in-plane lattice constant a, monolayer thickness t, cohesive energy E_c, in-plane elastic constants C_{ij}, and vacancy formation energies V_i. The monolayer thickness is defined as the center to center distance of the top and bottom atomic layers and is used in the calculation of elastic constants. N/A = not applicable; % Diff = percent difference.

	Ti₂C			Ti₃C₂			Ti₄C₃		
	DFT	BOP	% Diff	DFT	BOP	% Diff	DFT	BOP	% Diff
a (Å)	3.01	2.95	−2%	3.08	2.98	-3%	3.07	3.00	−2%
t (Å)	2.32	2.35	1%	4.97	4.82	−3%	7.13	7.29	2%
E_c (eV/atom)	−6.17	−6.34	3%	−6.71	−6.65	−1%	−6.90	−6.79	−2%
C_{11} (GPa)	625	636	2%	519	517	0%	504	494	−2%
C_{12} (GPa)	166	150	−10%	85	102	19%	98	110	12%
V_{Ti1} (eV)	N/A	N/A	N/A	11.51	11.46	0%	12.21	11.28	−8%
V_{Ti2} (eV)	7.71	8.64	12%	7.99	8.42	5%	7.72	8.44	9%
V_{C1} (eV)	N/A	N/A	N/A	N/A	N/A	N/A	9.47	9.55	1%
V_{C2} (eV)	10.64	11.37	7%	10.47	10.50	0%	10.19	10.53	3%

where F_f is the fracture force and r_{tip} is the radius of the indenter.

Atomistic nanoindentation simulations were performed by generating a circular MXene monolayer and fixing the positions of a thin ring of atoms on the perimeter. A 10 nm diameter spherical indenter was then introduced using a simple repulsive force of the following form:

$$F(r) = -K(r - r_{tip})^2, \quad (11)$$

where K is a force constant (10 ev/Å^3) and r is the distance from an atom to the center of the indenter. To generate force-displacement curves, the indenter was moved downward in a series of quasistatic steps, each with a displacement of 0.1 Å. Upon each movement of the indenter, atomic positions were relaxed via conjugate gradient (CG) minimization, followed by molecular dynamics at 1 K for 100 time steps (1 fs each) and, finally, a second CG minimization. The continuum model in Eq. (9) assumes a point load is applied, i.e., $r_{tip}/a < 0.03$ [49]. This is not an issue in experiments where films are typically two orders of magnitude larger than indenter tips, but it becomes an important consideration in atomistic simulations where the film size is limited by computational resources. As such, we have performed nanoindentation simulations on MXene monolayers ranging in diameter from 25 to 100 nm ($0.4 \geqslant r_{tip}/a \geqslant 0.1$). Thus, the force-displacement responses begin converging to that of a point load.

Figure 3(a) shows examples of the force-displacement curves generated from nanoindentation simulations of 100 nm diameter pristine MXene monolayers. Fits to Eq. (9) demonstrate that the atomistic data are well represented by the continuum model. From these curves it can be seen that as monolayer thickness increases, the maximum displacement decreases while the fracture force increases. A typical fracture pattern from one of these simulations is depicted in Fig. 3(b). The threefold symmetry corresponds to a fracture occurring along $\langle 1\bar{2}10 \rangle$ (zigzag) type directions. All three monolayer thicknesses fractured in a manner similar to this across the diameter range studied. Comparable fracture patterns have also been observed in experimental nanoindentations of MXene monolayers [11,12].

The 2D elastic modulus and breaking strength values extracted from fits to Eq. (9) are plotted as a function of monolayer diameter in Fig. 4. Due to the point-load assumption of the continuum model, the values begin to asymptotically converge as diameter increases. Therefore, we have fitted the data with a function of the form

$$f(d) = \frac{k_2}{d^2} + k_0, \quad (12)$$

where d is the monolayer diameter, k_2 is a constant, and k_0 represents the asymptote approached by the data. The choice of this functional form is based on the continuum model, which considers a 2D strain state and is therefore dependent on the film area (d^2) [47]. Figure 4 shows that the atomistic data have largely converged to the asymptotes at $d = 100$ nm. The values of k_0 for both the 2D elastic modulus and breaking strength are shown in Table II along with values for the modulus calculated from the in-plane elastic constants in Table I according to $(C_{11}^2 - C_{12}^2)/C_{11}$ [50,51]. The excellent agreement between the moduli calculated in two different ways

TABLE II. Asymptote values for the 2D elastic modulus and breaking strength of pristine MXene monolayers as determined from nanoindentation simulations. Values in parentheses are moduli calculated according to $(C_{11}^2 - C_{12}^2)/C_{11}$ for comparison. Values obtained via AFM experiments for $Ti_3C_2T_x$ in Ref. [11] are also shown for comparison.

	Ti_2C (BOP)	Ti_3C_2 (BOP)	$Ti_3C_2T_x$ (Expt.)	Ti_4C_3 (BOP)
E^{2D} (N/m)	132 (141)	248 (239)	326 ± 29	344 (342)
σ_{max}^{2D} (N/m)	22.1	32.3	17.0 ± 1.6	41.6

demonstrates the validity of the nanoindentation approach for characterizing 2D materials. Additionally, it is encouraging to see that the point-load assumption of the model can be reasonably approached with simulation sizes attainable by the BOP. Both the 2D elastic modulus and breaking strength increase as monolayer thickness increases. It is interesting to compare the values obtained here for Ti_3C_2 to those obtained experimentally for $Ti_3C_2T_x$ [11]. The experimentally measured 2D elastic modulus (326 ± 29 N/m) is significantly larger and can likely be attributed to the effects of surface terminations being present, which were previously shown to increase the stiffness of titanium carbide MXenes [15]. In contrast, the experimentally measured breaking strength (17.0 ± 1.6 N/m) is significantly reduced. This is likely attributable to the presence of vacancies, which are known to initiate fracture at lower strains [25,26].

Additional nanoindentation simulations on surface-terminated MXenes were attempted, but the resulting force-displacement curves were not well captured by the continuum model. Therefore, the calculated elastic and fracture properties from these simulations were unreliable. The origin of this behavior appears to stem from the large localized strains which occur directly beneath the indenter at large displacements (Fig. S3 [43]). These tend to rearrange the surface termination structure and thus the bonding character, given the prescribed limits of the potential, resulting in a departure from the continuum model. It is likely that this behavior could be mitigated by using a larger indenter, but this was not attempted as the indentation simulations would become more computationally expensive, and additional uniaxial tension and bending simulations can provide appropriate validation for surface-terminated MXenes.

B. Uniaxial tension

Compared to nanoindentation, tensile testing of 2D materials is much more difficult to achieve experimentally [52] and has been performed only on multilayer MXene nanosheets thus far [27,53]. Therefore, atomistic simulations are an ideal method to probe the tensile response of MXene monolayers. Uniaxial tension simulations were performed on 50×50 nm^2 MXene monolayers with loading along both the $\langle 1\bar{2}10 \rangle$ (zigzag) type and $\langle \bar{1}010 \rangle$ (armchair) type directions. Periodic boundary conditions were applied in plane with free surfaces out of plane. The simulation cell was thermally equilibrated at 300 K for 50 ps before uniaxial tension was performed at a strain rate of 10^8 s^{-1} until fracture. All uniaxial tension

TABLE III. Elastic modulus, tensile strength, and failure strain of pristine and surface-terminated MXene monolayers as calculated from the zigzag stress-strain curves.

	Zigzag, $n = 1$			Zigzag, $n = 2$			Zigzag, $n = 3$		
	Pristine	-O	-F	Pristine	-O	-F	Pristine	-O	-F
E^{2D} (N/m)	132	200	183	228	280	274	322	369	370
σ_{UTS} (N/m)	16.8	29.3	40.2	27.6	43.3	52.4	38.4	55.2	63.9
ϵ_f	0.168	0.222	0.347	0.179	0.213	0.318	0.191	0.216	0.315

simulations used a time step of 1 fs and ran within the *NPT* ensemble. A subset of the uniaxial tension simulations was also repeated on larger 100×100 nm^2 monolayers. Table S3 compares results at both sizes and clearly demonstrates size-independent results at this scale, thus justifying the choice of 50×50 nm^2 monolayers for the remaining simulations [43].

Figure 5 shows the stress-strain curves from the uniaxial tension simulations, and clearly, the surface terminations have significant effects on the mechanical response of the monolayers. The elastic modulus, tensile strength, and failure strain as determined from these curves are summarized in Tables III and IV. Overall, the addition of surface terminations leads to increases in all three properties, with -O terminations producing a more significant increase to elastic modulus and -F terminations producing more significant increases to tensile strength and failure strain. These results are in qualitative agreement with previous DFT calculations for Ti$_3$C$_2$T$_2$, albeit on much smaller systems [15]. The elastic moduli of the pristine monolayers as calculated from stress-strain curves are less than those calculated from the elastic constants in Table II. The origin of this discrepancy is likely the rippling that occurs in the freestanding monolayers upon thermal equilibration. Therefore, the initial stress-strain response is not purely due to in-plane stiffness.

Figure 6 shows snapshots of fracture from uniaxial tension simulations of Ti$_3$C$_2$ and Ti$_3$C$_2$T$_2$ ($n = 2$). Fracture of the $n = 1$ and $n = 3$ monolayers was qualitatively similar (Figs. S4 and S5 [43]). The pristine monolayers exhibit anisotropic fracture behavior consistent with the preferred fracture directions observed in nanoindentation simulations. When loading is applied in the zigzag direction, fracture occurs along lines about 60° from the loading axis. In contrast, when loading is applied in the armchair direction, fracture occurs along lines perpendicular to the loading axis. In both cases these correspond to fracture along zigzag type directions, as was the case in nanoindentation. The addition of surface terminations, in addition to increasing the strain and stress at which fracture occurs, has an influence on the frac-

ture mechanisms. For the -O terminated monolayers, fracture initiates along zigzag type directions, but it does not proceed without obstruction as it does in the pristine monolayers. This leads to jagged fracture surfaces rather than sharp atomic planes. These observations are consistent with the recent ReaxFF simulations on much smaller systems by Li *et al.*, who noted the ability of -O terminations to impede crack propagation [27]. We observed a similar mechanism with -F surface terminations, albeit to a lesser extent due to Ti-F bonds being weaker than Ti-O bonds.

C. Bending

While a number of experimental and modeling studies have been devoted to characterizing the in-plane mechanical response of MXenes, only a few have investigated the out-of-plane mechanical response [18,23]. Specifically, the bending rigidity of MXenes is of great interest for their use in applications requiring both strength and flexibility. As such, the molecular statics approach described by Lu *et al.* [54] was used to calculate bending rigidity for pristine and surface-terminated MXene monolayers. This method maps the atoms of a planar monolayer onto cylinders of decreasing radius, effectively nanotubes, and subsequently calculates the strain energy as a function of curvature. In the linear elastic regime, this relation can be expressed as follows:

$$W = \tfrac{1}{2}D\kappa^2, \tag{13}$$

where W is the strain energy (excess total energy relative to a flat monolayer) per unit area, κ is the radius of curvature, and D is the bending rigidity. Bending simulations were performed with cylinders oriented along both the zigzag and armchair directions, but as has been shown for other hexagonal 2D materials [54,55], bending rigidity is isotropic and was thus identical for both orientations.

Figure 7(a) shows data from these bending simulations for pristine MXene monolayers plotted along with fits to Eq. (13) (see Fig. S6 for surface-terminated data [43]). The excellent agreement of the fits demonstrates the validity of

TABLE IV. Elastic modulus, tensile strength, and failure strain of pristine and surface-terminated MXene monolayers as calculated from the armchair stress-strain curves.

	Armchair, $n = 1$			Armchair, $n = 2$			Armchair, $n = 3$		
	Pristine	-O	-F	Pristine	-O	-F	Pristine	-O	-F
E^{2D} (N/m)	133	204	185	223	284	277	324	374	371
σ_{UTS} (N/m)	19.6	25.3	28.7	30.6	36.1	48.5	41.4	49.4	58.4
ϵ_f	0.201	0.236	0.317	0.197	0.206	0.317	0.197	0.215	0.298

TABLE V. Bending rigidity of pristine and surface-terminated MXene monolayers calculated from fits to Eq. (13).

	D (eV)		
	Pristine	-O	-F
Ti_2CT_x	9.81	28.8	18.9
$Ti_3C_2T_x$	43.3	86.5	72.7
$Ti_4C_3T_x$	122	194	181

Eq. (13) in the range of curvatures tested. Surface-terminated sheets exhibited a departure from Eq. (13) at large curvatures (Fig. S6 [43]), and thus, fits were confined to smaller curvature values. The calculated bending rigidity for both pristine and surface-terminated monolayers is shown in Table V. Both types of surface termination increase bending rigidity relative to a pristine monolayer, with -O terminations providing the larger increase, as was the case for in-plane stiffness. Figure 7(b) plots bending rigidity for all monolayers as a function of thickness cubed, which gives a roughly linear relationship according to the continuum theory of thin plates. This plot indicates that while surface terminations increase bending rigidity relative to pristine monolayers, they would be less rigid than a hypothetical pristine monolayer of comparable thickness. This follows from the fact that the Ti-T bonds are not as strong as Ti-C bonds, so adding additional layers of the latter has a larger impact on bending rigidity. The trends in the bending data reported here are in good agreement with DFT calculations [18].

IV. SIMULATING DEFECTED MXENE MONOLAYERS

As a final demonstration of the utility of the BOP, we have performed additional large-scale uniaxial tension simulations on more realistic MXene monolayers containing random distributions of both vacancies and nonuniform surface terminations. For each thickness ($n = 1, 2,$ or 3), five different monolayers were created in order to generate more statistics. We utilize the same vacancy concentration (3%) and surface termination site occupation ratios (8% for -O and 3% for -F) as Li *et al.* in their recent ReaxFF simulations [27]. Loading was applied along the zigzag direction until fracture, with the same uniaxial tension simulation parameters used previously. Representative stress-strain curves from these simulations are shown in Fig. 8(a), and Table VI shows the calculated elastic modulus, tensile strength, and failure strain. All three properties are reduced from those of the pristine case (Table III).

This was demonstrated previously for elastic modulus as a result of Ti and C vacancies [25]. The presence of additional surface terminations could likely compensate for this effect, but evidently, the site occupation used here was too low to have a noticeable impact on stiffness. The tensile strength and failure strain are reduced more significantly, which we attribute to the preferential nucleation of cracks at various vacancy clusters.

Snapshots from one of the simulations on a Ti_2CT_x monolayer are shown in Figs. 8(b)–8(d). As suspected, they implicate vacancy clusters in the crack nucleation and propagation process. In Fig. 8(b), several vacancy clusters (orange circles) in close proximity to one another are depicted. At this point in the simulation, the applied strain has pulled them apart enough to appear as significantly sized holes in the monolayer. Further strain nucleates a crack at the vacancy clusters [Fig. 8(c)], which then rapidly propagates across the entirety of the monolayer [Fig. 8(d)]. We note that the propagating crack does not follow a mostly straight line as it tended to do in pristine monolayers (Fig. 6) but rather appears quite jagged as a result of the high concentration of vacancies, which attract the growing crack. Similar crack nucleation and propagation mechanisms were observed in $Ti_3C_2T_x$ and $Ti_4C_3T_x$ monolayers. These simulations demonstrate that the BOP can successfully model more realistic MXene monolayers, thus enabling more detailed characterizations of how various concentrations and distributions of both vacancies and surface terminations can impact mechanical properties. This will only increase the already impressive tunability of properties exhibited by MXenes and will be the subject of future work.

V. CONCLUSIONS

We have developed a BOP for titanium carbide MXenes which can successfully model both pristine and surface-terminated monolayers. Its predictions of relevant structural, elastic, and defect properties, as well as trends in properties imparted by surface terminations, are in good agreement with DFT calculations. The simple functional form of the BOP enables scalable atomistic simulations an order of magnitude larger than was previously possible, which importantly produce size-independent results with respect to mechanical properties. This was demonstrated with large-scale simulations of nanoindentation, uniaxial tension, and bending, which provide insights into the elastic and fracture behaviors of titanium carbide MXenes and how they are influenced by surface terminations. Overall, thicker monolayers exhibit

TABLE VI. Average elastic modulus, tensile strength, and failure strain of MXene monolayers containing vacancies and nonuniform surface terminations as calculated from uniaxial tension simulations. Uncertainties are determined from the standard deviations in the properties of the five different monolayers created for each system. Values in parentheses indicate the percent differences of the average values from corresponding values of pristine monolayers in Table III.

	Ti_2CT_x	$Ti_3C_2T_x$	$Ti_4C_3T_x$
E^{2D} (N/m)	116 ± 1 (−12%)	206 ± 1 (−10%)	291 ± 1 (−10%)
σ_{UTS} (N/m)	9.3 ± 0.1 (−45%)	17.3 ± 0.8 (−37%)	27.3 ± 0.6 (−29%)
ϵ_f	0.099 ± 0.001 (−41%)	0.105 ± 0.007 (−41%)	0.124 ± 0.004 (−35%)

increased in-plane stiffness and strength but reduced out-of-plane flexibility. The same was observed through the addition of either -O or -F surface terminations. Of great importance is the ability of the BOP to model more realistic MXene monolayers with distributions of vacancies and nonuniform surface terminations. These variables can have significant effects on mechanical properties and deformation mechanisms and can now be studied in greater detail. For example, here we demonstrated the deleterious effects that high concentrations of vacancies can have on MXene mechanical properties. MXenes are prized as 2D materials with highly tunable properties, but characteristic variables such as vacancies have been largely overlooked compared to chemistry. Therefore, utilizing large-scale atomistic simulations to better understand the influence of vacancy and surface termination distributions should result in even greater property-tuning capabilities and help to inform synthesis and postprocessing techniques to this end.

The BOP described herein is intended for use on monolayers of titanium carbide MXenes. This system was chosen simply because it has been the most studied to date. The success of the BOP here, however, suggests that it could be readily adapted to other MXene compositions of interest, provided sufficient experimental and DFT data are available for fitting. Modeling multilayer MXenes, which is of crucial importance for studying tribological properties, should also be possible through the addition of a separate interlayer potential, as has been done in several instances for graphite [56–58]. Clearly, there are numerous possibilities for using BOPs to construct large-scale atomistic simulations of MXenes and to increase our fundamental knowledge of their unique and tunable properties and deformation behavior.

APPENDIX: BOP INTERACTION PARAMETERS

Fitted parameters for the $Ti_{n+1}C_nT_x$ MXene BOP are shown in Tables VII, VIII, and IX.

TABLE VII. BOP parameters for elemental interactions in $Ti_{n+1}C_nT_x$ MXenes. Ti-Ti parameters were previously developed [29], while C-C and O-O/F-F parameters are adapted from Refs. [34,35], respectively.

Parameter	Ti-Ti	C-C	O-O/F-F
λ_3	0.590960	0.000000	0.000000
γ	0.001963	0.112330	0.825950
c	1.356500	181.910000	0.035608
d	0.230100	6.284330	0.046496
h	−0.904680	−0.555600	−0.450560
λ_2	1.367849	1.930901	2.773286
B	184.973776	175.426651	527.650509
λ_1	1.940020	4.184262	3.844884
A	540.866546	2019.844901	1388.081581
R	3.580900	2.000000	2.000000
D	0.302900	0.150000	0.200000

TABLE VIII. BOP parameters for binary interactions in $Ti_{n+1}C_nT_x$ MXenes. In the notation for the λ_3 parameters, the first two elements represent the bond of interest, while the third represents the atom influencing this bond. Therefore, entries with the order of the first two elements swapped are omitted as they are equivalent to the unswapped entries.

Parameter	Ti-C	Ti-O	Ti-F
$\lambda_3(Ti, Ti, X)$	0.446458	0.412123	0.200289
$\lambda_3(Ti, X, X)$	0.700860	0.954584	0.188395
$\lambda_3(Ti, X, Ti)$	1.089256	0.849853	0.458645
$\lambda_3(X, X, Ti)$	1.302977	0.101516	0.018686
γ	0.000145	0.198828	0.349488
c	64.682013	0.090216	0.270729
d	0.902079	0.193661	0.366691
h	-0.012386	-0.043538	0.133742
λ_2	0.982312	2.666001	2.648741
B	28.999542	1552.074486	2264.428088
λ_1	3.075488	6.081160	4.915356
A	417.942094	414001.976910	78916.885953
R	3.000000	3.000000	3.000000
D	0.150000	0.200000	0.150000

TABLE IX. Ternary BOP parameters for $Ti_{n+1}C_nT_x$ MXenes. See the caption of Table VIII for an explanation of the λ_3 notation.

Parameter	Value
$\lambda_3(Ti, C, O)$	1.049389
$\lambda_3(Ti, O, C)$	0.243830
$\lambda_3(Ti, C, F)$	1.050089
$\lambda_3(Ti, F, C)$	0.425833

[1] B. Anasori and Y. Gogotsi, *2D Metal Carbides and Nitrides (MXenes)* (Springer Nature, Switzerland, 2019).

[2] B. Anasori, M. R. Lukatskaya, and Y. Gogotsi, 2D metal carbides and nitrides (MXenes) for energy storage, Nat. Rev. Mater. **2**, 16098 (2017).

[3] Z. Li and Y. Wu, 2D early transition metal carbides (MXenes) for catalysis, Small **15**, 1804736 (2019).

[4] A. Morales-García, F. Calle-Vallejo, and F. Illas, MXenes: New horizons in catalysis, ACS Catal. **10**, 13487 (2020).

[5] H. Kim and H. N. Alshareef, MXetronics: MXene-enabled electronic and photonic devices, ACS Mater. Lett. **2**, 55 (2020).

[6] E. Lee and D.-J. Kim, Recent exploration of two-dimensional MXenes for gas sensing: From a theoretical to an experimental view, J. Electrochem. Soc. **167**, 037515 (2020).

[7] S. Thomas and M. Asle Zaeem, Phosgene gas sensing of Ti_2CT_2 (T = F$^-$, O$^-$, OH$^-$) MXenes, Advanced Theory and Simulations **4**, 2000250 (2021).

[8] M. Malaki and R. S. Varma, Mechanotribological aspects of MXene-reinforced nanocomposites, Adv. Mater. **32**, 2003154 (2020).

[9] S. Yazdanparast, S. Soltanmohammad, A. Fash-White, G. J. Tucker, and G. L. Brennecka, Synthesis and surface chemistry of 2D TiVC solid-solution MXenes, ACS Appl. Mater. Interfaces **12**, 20129 (2020).

[10] B. C. Wyatt, A. Rosenkranz, and B. Anasori, 2D MXenes: Tunable mechanical and tribological properties, Adv. Mater. **33**, 2007973 (2021).

[11] A. Lipatov, H. Lu, M. Alhabeb, B. Anasori, A. Gruverman, Y. Gogotsi, and A. Sinitskii, Elastic properties of 2D $Ti_3C_2T_x$ MXene monolayers and bilayers, Sci. Adv. **4**, eaat0491 (2018).

[12] A. Lipatov, M. Alhabeb, H. Lu, S. Zhao, M. J. Loes, N. S. Vorobeva, Y. Dall'Agnese, Y. Gao, A. Gruverman, Y. Gogotsi, and A. Sinitskii, Electrical and elastic properties of individual single-layer $Nb_4C_3T_x$ MXene flakes, Adv. Electron. Mater. **6**, 1901382 (2020).

[13] M. Kurtoglu, M. Naguib, Y. Gogotsi, and M. W. Barsoum, First principles study of two-dimensional early transition metal carbides, MRS Commun. **2**, 133 (2012).

[14] Z. Guo, J. Zhou, C. Si, and Z. Sun, Flexible two-dimensional $Ti_{n+1}C_n$ (n = 1, 2 and 3) and their functionalized MXenes predicted by density functional theories, Phys. Chem. Chem. Phys. **17**, 15348 (2015).

[15] Z. H. Fu, Q. F. Zhang, D. Legut, C. Si, T. C. Germann, T. Lookman, S. Y. Du, J. S. Francisco, and R. F. Zhang, Stabilization and strengthening effects of functional groups in two-dimensional titanium carbide, Phys. Rev. B **94**, 104103 (2016).

[16] U. Yorulmaz, A. Özden, N. K. Perkgöz, F. Ay, and C. Sevik, Vibrational and mechanical properties of single layer MXene structures: A first-principles investigation, Nanotechnology **27**, 335702 (2016).

[17] N. Zhang, Y. Hong, S. Yazdanparast, and M. Asle Zaeem, Superior structural, elastic and electronic properties of 2D titanium nitride MXenes over carbide MXenes: A comprehensive first principles study, 2D Mater. **5**, 045004 (2018).

[18] T. Hu, J. Yang, W. Li, X. Wang, and C. M. Li, Quantifying the rigidity of 2D carbides (MXenes), Phys. Chem. Chem. Phys. **22**, 2115 (2020).

[19] X. Sang, Y. Xie, M.-W. Lin, M. Alhabeb, K. L. Van Aken, Y. Gogotsi, P. R. C. Kent, K. Xiao, and R. R. Unocic, Atomic defects in monolayer titanium carbide ($Ti_3C_2T_x$) MXene, ACS Nano **10**, 9193 (2016).

[20] M. A. Hope, A. C. Forse, K. J. Griffith, M. R. Lukatskaya, M. Ghidiu, Y. Gogotsi, and C. P. Grey, NMR reveals the surface functionalisation of Ti_3C_2 MXene, Phys. Chem. Chem. Phys. **18**, 5099 (2016).

[21] J. Halim, K. M. Cook, M. Naguib, P. Eklund, Y. Gogotsi, J. Rosen, and M. W. Barsoum, X-ray photoelectron spectroscopy of select multi-layered transition metal carbides (MXenes), Appl. Surf. Sci. **362**, 406 (2016).

[22] V. N. Borysiuk, V. N. Mochalin, and Y. Gogotsi, Molecular dynamic study of the mechanical properties of two-dimensional titanium carbides $Ti_{n+1}C_n$ (MXenes), Nanotechnology **26**, 265705 (2015).

[23] V. N. Borysiuk, V. N. Mochalin, and Y. Gogotsi, Bending rigidity of two-dimensional titanium carbide (MXene) nanoribbons: A molecular dynamics study, Comput. Mater. Sci. **143**, 418 (2018).

[24] N. C. Osti, M. Naguib, A. Ostadhossein, Y. Xie, P. R. C. Kent, B. Dyatkin, G. Rother, W. T. Heller, A. C. T. Van Duin, Y. Gogotsi, and E. Mamontov, Effect of metal ion intercalation on the structure of MXene and water dynamics on its internal surfaces, ACS Appl. Mater. Interfaces **8**, 8859 (2016).

[25] G. Plummer, B. Anasori, Y. Gogotsi, and G. J. Tucker, Nanoindentation of monolayer $Ti_{n+1}C_nT_x$ MXenes via atomistic simulations: The role of composition and defects on strength, Comput. Mater. Sci. **157**, 168 (2019).

[26] Y. I. Jhon, Y. T. Byun, J. H. Lee, and Y. M. Jhon, Robust mechanical tunability of 2D transition metal carbides via surface termination engineering: Molecular dynamics simulation, Appl. Surf. Sci. **532**, 147380 (2020).

[27] Y. Li, C. Wei, S. Huang, A. Ghasemi, W. Gao, C. Wu, and V. N. Mochalin, *In situ* tensile testing of nanometer-thick two-dimensional transition-metal carbide films: Implications for MXenes acting as nanoscale reinforcement agents, ACS Applied Nano Mater. **4**, 5058 (2021).

[28] T. P. Senftle, S. Hong, M. M. Islam, S. B. Kylasa, Y. Zheng, Y. K. Shin, C. Junkermeier, R. Engel-Herbert, M. J. Janik, H. M. Aktulga, T. Verstraelen, A. Grama, and A. C. T. van Duin, The ReaxFF reactive force-field: Development, applications and future directions, npj Comput. Mater. **2**, 15011 (2016).

[29] G. Plummer and G. J. Tucker, Bond-order potentials for the Ti_3AlC_2 and Ti_3SiC_2 MAX phases, Phys. Rev. B **100**, 214114 (2019).

[30] G. Plummer, H. Rathod, A. Srivastava, M. Radovic, T. Ouisse, M. Yildizhan, P. O. Å. Persson, K. Lambrinou, M. W. Barsoum, and G. J. Tucker, On the origin of kinking in layered crystalline solids, Mater. Today **43**, 45 (2021).

[31] J. Tersoff, New empirical approach for the structure and energy of covalent systems, Phys. Rev. B **37**, 6991 (1988).

[32] K. Albe, K. Nordlund, J. Nord, and A. Kuronen, Modeling of compound semiconductors: Analytical bond-order potential for Ga, As, and GaAs, Phys. Rev. B **66**, 035205 (2002).

[33] N. Juslin, P. Erhart, P. Träskelin, J. Nord, K. O. E. Henriksson, K. Nordlund, E. Salonen, and K. Albe, Analytical interatomic potential for modeling nonequilibrium processes in the W–C–H system, J. Appl. Phys. **98**, 123520 (2005).

[34] P. Erhart and K. Albe, Analytical potential for atomistic simulations of silicon, carbon, and silicon carbide, Phys. Rev. B **71**, 035211 (2005).

[35] P. Erhart, N. Juslin, O. Goy, K. Nordlund, R. Müller, and K. Albe, Analytic bond-order potential for atomistic simulations of zinc oxide, J. Phys.: Condens. Matter **18**, 6585 (2006).

[36] G. Kresse and J. Furthmüller, Efficient iterative schemes for *ab initio* total-energy calculations using a plane-wave basis set, Phys. Rev. B **54**, 11169 (1996).

[37] J. P. Perdew, K. Burke, and M. Ernzerhof, Generalized Gradient Approximation Made Simple, Phys. Rev. Lett. **77**, 3865 (1996).

[38] P. E. Blöchl, Projector augmented-wave method, Phys. Rev. B **50**, 17953 (1994).

[39] J. C. Lagarias, J. A. Reeds, M. H. Wright, and P. E. Wright, Convergence properties of the Nelder–Mead simplex method in low dimensions, SIAM J. Optim. **9**, 112 (1998).

[40] S. Thomas, O. Hildreth, and M. Asle Zaeem, Unveiling the role of atomic defects on the electronic, mechanical and elemental diffusion properties in CuS, Scr. Mater. **192**, 94 (2021).

[41] S. Thomas, A. K. Madam, and M. Asle Zaeem, From fundamental to CO_2 and $COCl_2$ gas sensing properties of pristine and defective Si_2BN monolayers, Phys. Chem. Chem. Phys. **24**, 4394 (2022).

[42] A. P. Thompson, H. M. Aktulga, R. Berger, D. S. Bolintineanu, W. M. Brown, P. S. Crozier, P. J. in't Veld, A. Kohlmeyer, S. G. Moore, T. D. Nguyen, R. Shan, M. J. Stevens, J. Tranchida, C. Trott, and S. J. Plimpton, LAMMPS—A flexible simulation tool for particle-based materials modeling at the atomic, meso, and continuum scales, Comput. Phys. Commun. **271**, 108171 (2022); LAMMPS, https://lammps.org/.

[43] See Supplemental Material at http://link.aps.org/supplemental/10.1103/PhysRevB.106.054105 for further information on the surface termination fitting results and large-scale simulations.

[44] A. Togo and I. Tanaka, First principles phonon calculations in materials science, Scr. Mater. **108**, 1 (2015).

[45] L. T. Kong, Phonon dispersion measured directly from molecular dynamics simulations, Comput. Phys. Commun. **182**, 2201 (2011).

[46] A. Stukowski, Visualization and analysis of atomistic simulation data with OVITO–The open visualization tool, Modell. Simul. Mater. Sci. Eng. **18**, 015012 (2010).

[47] C. Lee, X. Wei, J. W. Kysar, and J. Hone, Measurement of the elastic properties and intrinsic strength of monolayer graphene, Science **321**, 385 (2008).

[48] S. Bertolazzi, J. Brivio, and A. Kis, Stretching and breaking of ultrathin MoS_2, ACS Nano **5**, 9703 (2011).

[49] X. Tan, J. Wu, K. Zhang, X. Peng, L. Sun, and J. Zhong, Nanoindentation models and Young's modulus of monolayer graphene: A molecular dynamics study, Appl. Phys. Lett. **102**, 071908 (2013).

[50] J. Zhou and R. Huang, Internal lattice relaxation of single-layer graphene under in-plane deformation, J. Mech. Phys. Solids **56**, 1609 (2008).

[51] X. Wei, B. Fragneaud, C. A. Marianetti, and J. W. Kysar, Nonlinear elastic behavior of graphene: *Ab initio* calculations to continuum description, Phys. Rev. B **80**, 205407 (2009).

[52] P. Zhang, L. Ma, F. Fan, Z. Zeng, C. Peng, P. E. Loya, Z. Liu, Y. Gong, J. Zhang, X. Zhang, P. M. Ajayan, T. Zhu, and J. Lou, Fracture toughness of graphene, Nat. Commun. **5**, 3782 (2014).

[53] K. L. Firestein, J. E. von Treifeldt, D. G. Kvashnin, J. F. S. Fernando, C. Zhang, A. G. Kvashnin, E. V. Podryabinkin, A. V. Shapeev, D. P. Siriwardena, P. B. Sorokin, and D. Golberg, Young's modulus and tensile strength of Ti_3C_2 MXene nanosheets as revealed by in situ TEM probing, AFM nanomechanical mapping, and theoretical calculations, Nano Lett. **20**, 5900 (2020).

[54] Q. Lu, M. Arroyo, and R. Huang, Elastic bending modulus of monolayer graphene, J. Phys. D **42**, 102002 (2009).

[55] J.-W. Jiang, Z. Qi, H. S. Park, and T. Rabczuk, Elastic bending modulus of single-layer molybdenum disulfide (MoS_2): Finite thickness effect, Nanotechnology **24**, 435705 (2013).

[56] S. J. Stuart, A. B. Tutein, and J. A. Harrison, A reactive potential for hydrocarbons with intermolecular interactions, J. Chem. Phys. **112**, 6472 (2000).

[57] A. N. Kolmogorov and V. H. Crespi, Registry-dependent interlayer potential for graphitic systems, Phys. Rev. B **71**, 235415 (2005).

[58] M. Wen, S. Carr, S. Fang, E. Kaxiras, and E. B. Tadmor, Dihedral-angle-corrected registry-dependent interlayer potential for multilayer graphene structures, Phys. Rev. B **98**, 235404 (2018).